Journal of Organometallic Chemistry 881 (2019) 66–78

Contents lists available at ScienceDirect

Journal of Organometallic Chemistry

journal homepage: www.elsevier.com/locate/jorganchem

Ruthenium(II)-arene complexes with monodentate aminopyridine ligands: Insights into redox stability and electronic structures and biological activity ☆

Flávia Marszaukowski [a], Ivelise Dimbarre Lao Guimarães [a], Juliana Paula da Silva [a], Luis Henrique da Silveira Lacerda [a], Sergio Ricardo de Lazaro [a], Márcio Peres de Araujo [b], Patrícia Castellen [a], Tania Toyomi Tominaga [c], René T. Boeré [d], Karen Wohnrath [a, *]

[a] *Departamento de Química, Universidade Estadual de Ponta Grossa, Av. Gal. Carlos Cavalcanti, 4748, Uvaranas, CEP, 84030-900, Ponta Grossa, PR, Brazil*
[b] *Departamento de Química, Universidade Federal do Paraná, Rua Coronel Francisco Heraclito dos Santos, 100 - Jardim das Américas, CEP, 81531-990, Curitiba, PR, Brazil*
[c] *Departamento de Física, Universidade Estadual do Centro-Oeste, Rua Simeão Camargo Varela de Sá, 03, Vila Carli, CEP, 85040-080, Guarapuava, PR, Brazil*
[d] *Department of Chemistry and Biochemistry, University of Lethbridge, 4401University Drive, Lethbridge, Alberta, Canada, T1K 3M4*

ARTICLE INFO

Article history:
Received 4 September 2018
Received in revised form
28 November 2018
Accepted 30 November 2018
Available online 4 December 2018

Keywords:
Ruthenium(II)-Arene
Pyridine ligands
DNA interaction
BSA interaction
Cytotoxicity
Crystal structure

ABSTRACT

The synthesis and spectroscopic characterization of four ruthenium(II) arene complexes with monodentate pyridine derivatives ([(η^6–*p*-cymene)$RuCl_2L$]: L = 2-aminopyridine, 2-methylaminopyridine, 2-benzylaminopyridine, and pyridine) are reported. Full characterization was undertaken using ^1H and ^{13}C NMR spectroscopy, vibrational and electronic spectroscopies and crystallography (2-methylaminopyridine derivative). UB3LYP//(6-31 + G(d),SPK-DZCD) density functional theory calculations determined the molecular and electronic structures. Cyclic voltammetry determined a large electrochemical stability window (>2.2 V) extending well beyond the physiological E°. Interactions with CT-DNA and BSA, and activity against four cell lines (HeLa, B16F10, HEp-2 and Vero) were evaluated. The 2-methylaminopyridine shows weak cytotoxicity ($IC_{50} = 346\ \mu mol\ L^{-1}$) towards HeLa cells. All the complexes interact with DNA at relatively high concentrations as determined by UV–vis spectroscopic titration. Results of circular dichroism spectroscopy, ethidium bromide competition, fluorescence spectroscopy and DNA viscosity measurements identify electrostatic interactions between partly hydrolyzed cationic complexes and the phosphate backbone of DNA as the most likely interaction mode. Slower rates of hydrolysis may be the origin of lower cytotoxicity for κ^1 these complexes.

1. Introduction

Interest in utilizing ruthenium-based metal complexes as vital new drugs for the treatment of cancer, either to replace platinum therapies where resistance has developed or to expand the therapeutic range of tumor types, remains very strong [1–9]. Whereas all the platinum-based drugs in clinical use are based on square-planar L_2PtCl_2 in the classic *cis* configuration, the range of structures, ligand-types and geometries of ruthenium complexes which have demonstrated anti-proliferative action is extremely diverse. In this regard, a strong warning has recently been given against making false generalizations (low toxicity because of similarity to iron; slow rates of ligand exchange; activation is by reduction to Ru(II); specific accumulation in cancerous tissues; uptake mediated by transferrin) about ruthenium cytotoxic agents [7]. In short, different types of ruthenium-based metallodrugs are under investigation, with distinctive behaviors. One class of ruthenium complex that differs significantly in structure and properties from the platinum-type agents are (η^6-arene)ruthenium(II) tripodal organometallic complexes, the vast majority of which have either one (type A) or two (type B: E = NR) nitrogen donor ligands (Chart 1).

☆ Supplementary information (SI) available: X-ray crystallography data; DFT computed and crystallographic structure depictions; vibrational spectroscopic data; archival NMR data; Uv–vis spectroscopic data; solubility and stability of the complexes; additional cyclic voltammograms and scan-rate studies; biological data and literature survey; Cartesian coordinates of DFT geometries. CCDC 1822445; SI and crystallographic data in CIF.

* Corresponding author.
E-mail address: kawoh@uepg.br (K. Wohnrath).

https://doi.org/10.1016/j.jorganchem.2018.11.036

Abbreviations table

B16F10	Murine melanoma cell line;
BSA	Bovine serum albumin
CT-DNA	Calf-Thymus deoxyribonucleic acid
DMSO	Dimethyl sulfoxide;
EtBr	Ethidium bromide
HeLa	Cervical carcinoma cell line
HEp-2	Laryngeal carcinoma cell line
PBS	Phosphate buffer
RAPTA	Ruthenium arene PTA
TBAP	Tetrabutylammonium perchlorate
Vero	Kidney murine cell line

The remaining coordination sites are almost always occupied by chlorides. The type A complexes are thus neutral ruthenium complexes with κ^1-pyridyl ligands [1]. In the chelated type B complexes, the second donor group "E" is frequently nitrogen but can also be oxygen or carbon moieties [5]. There are now numerous derivates of type A where the nitrogen ligand is a simple pyridine group [10–19].

In the first step of a larger research program utilizing pyridine-based ligands of both types A and B, we wished to investigate the cytotoxicity of a selected series of simple neutral 2-aminopyridine complexes incorporating the ligands 2-aminopyridine (**apy**), 2-methylaminopyridine **(meapy)** and 2-benzylaminopyridine **(bzapy)** (Chart 1). 2-Aminopyridines are important nitrogen-containing ligands due to a strong nitrogen donor in the ring, while the aromatic amino substituent provides additional electronic and hydrogen-bonding stability. Such complexes have attracted considerable interest recently because of their applications in pharmaceutical research, for instance glucokinase activators [20] or selective inhibitors of neuronal nitric oxide synthase [21]. Herein we report on the synthesis, structures and biological activity of four $[(\eta^6\text{-}p\text{-cymene})RuCl_2L]$ complexes **1**–**3** where L = **apy, meapy and bzapy**, respectively. In addition to cytotoxicity tests *in vitro* against cancer and normal cell lines (HeLa, B16F10, HEp-2 and Vero), studies on the interaction of the complexes with DNA and BSA were undertaken to search for understanding of biological activity. The long-known complex **4** of the parent ligand **py** was included for comparison to the aminopyridines [13,22–25]. Complex **4** did not display any cytotoxic effect as previously reported in the literature [26].

While this work was in progress, studies of a number of other type-A pyridine complexes appeared in the literature [24–28]. The biological properties of these analogues, in particular the substituted 2-phenylaminopyridine derivatives reported by Richter et al. [27], serve as interesting parallels to our results. By incorporating remote carboxylate donor groups at the 4-position of the NC_6H_4X rings, moderate antiproliferative activity was observed. A comparison of this closely parallel series with **1** to **4** (i.e. with and without these remote donor groups) proved helpful for delineating their structure-property relationships.

Quantum calculations on ruthenium complexes are relatively rare in the literature but there has been an increase in interest in using such methods to investigate molecular structures [29,30] and catalysis [31] of Ru complexes. Kreitner and co-authors applied Density Functional Theory (DFT) in a study of excited state behaviour of cyclometalated *bis*(tridentate)ruthenium(II) complexes [32], while Das and co-authors investigated the interaction of aquated ruthenium(III) complexes with DNA base pairs using computational methods [33]. Herein we employ DFT computational methods to provide a basic understanding of the electronic structures of the title complexes to provide insights into their spectroscopic and redox behaviours *in vitro* and in vivo. To date, these aspects of ruthenium-arene complexes have been unduly ignored despite an intensive literature regarding their potential utility, or otherwise, as new antiproliferative agents.

2. Experimental section

2.1. Materials and general methods

$RuCl_3 \cdot 3H_2O$ was purchased from Strem and the precursor complex $[\{(\eta^6\text{-}p\text{-cymene})Ru(\mu\text{-}Cl)Cl\}_2]$ was prepared according to published procedures [34,35]. Ligands **apy**, **meapy, bzapy** and **py**, as well as α-phellandrene, calf thymus DNA (CT-DNA), bovine serum albumin (BSA) and tetrabutylammonium perchlorate (TBAP) were purchased from Sigma-Aldrich and used without further purification. The solvents were rigorously purified by standard procedures [36]. All synthesis manipulations were carried out under an argon atmosphere using modified Schlenk techniques.

2.2. Physical measurements

FT-IR spectra (4000-550 cm^{-1}) were recorded on a DRS-8000/Shimadzu IRPrestige-21 spectrometer. Raman spectra (40-4400 cm^{-1}) were obtained with a Bruker Senterra dispersive Raman microscope. UV–vis spectra (0.1 mmol) were recorded on a Varian Cary 50 Bio spectrophotometer using quartz cells, in the range 200–900 nm. Conductivity values were obtained using an Infolab WTW TetraCon® 325 conductivity bridge in a thermostated bath held at 25.0 °C. Aqueous solution of $1 \cdot 10^{-3}$ mol L^{-1} NaCl was used as the 1:1 electrolyte standard, where the conductivity value for this solution was 124.7 µS cm^{-1} $[^nBu_4N][ClO_4]$ was used similarly used as the standard in CH_3CN, for which the molar conductance is 197.1 µS cm^{-1} [37]. X-ray crystallography was undertaken for complex **2** using Cu K_α radiation at 100 K on a Rigaku-Oxford Diffraction SuperNova diffractometer equipped with a Pilatus 200K HPAD detector. Details of the structure solution and refinement are provided in the SI. The structure is complicated by wholesale disorder of the **meapy** ligand, presence of $CHCl_3$ solvent and $Z' = 2$. CCDC 1822445 contains the supplementary crystallographic data for this paper.

1D and 2D solution-phase NMR experiments (^1H, ^{13}C, ^1H–^1H gCOSY,^1H–^{13}C gHSQC, and ^1H–^{13}C gHMBC) were recorded on a Bruker Model DRX, 400 MHz spectrometer, at probe temperature using, in general, 20 mg samples of complexes dissolved in $CDCl_3$, containing a trace amount of tretramethylsilane (TMS) that was used as an internal reference (0 ppm). The ^1H and ^{13}C NMR spectra were acquired with 16 and 2048 scans; spectral widths (sw) of 6393.862 and 25510.203 Hz; relaxation delays (d1) of 1 and 0.2 s; and 90° and 80° pulse lengths, respectively. The ^1H–^1H gCOSY, ^1H–^{13}C gHSQC and ^1H–^{13}C gHMBC, spectra were acquired with 8, 16, and 8 scans and spectral widths of 4595.588 for F2 and 18852.455 for F1, respectively. The relaxation delay of 1 s, with 256 data points at F1 and 4 K at F2 were the same in all 2D NMR experiments. Archival spectral data is presented in the SI.

2.3. Computational methodology

DFT calculations in gas phase, zero Kelvin and vacuum were carried out on **1** as an electronic model for all the complexes and on **2** to verify the geometry due to the disorder encountered in the X-ray diffraction study. All models were fully optimized from 10^{-6} Hartree and 10^{-8} Hartree for self-consistent field (SCF) based on the Hartree-Fock formalism and total energy criteria, respectively.

Harmonic frequency calculations were undertaken to confirm that the geometries are at least local minima on the potential energy surface. Similar calculations were undertaken for **1**$^{+}$ (doublet), **1**$^{2+}$ (singlet and triplet), **1**$^{-}$ (doublet) and **1**$^{2-}$ (singlet and triplet) to help interpret the voltammetry results. In this study, all calculations were performed on GAUSSIAN09 program using B3LYP [38] functional with Gaussian-type 6-31 + G(d) basis set for C, H, N, P, and F atoms; whereas the all-electron, relativistically corrected, Sapporo double-zeta (SPK-DZCD) basis set was applied to describe the Ru atom [39].

2.4. *Electrochemistry*

Cyclic voltammetric experiments were recorded on a potentiostat/galvanostat µAutolab (Type III, Metrohm-Eco Chemie) connected to a computer with GPES 4.9 (General Purpose Electrochemical System) software. The measurements were performed in nitrogen atmosphere at room temperature in dry CH_3CN with tetrabutylammonium perchlorate (TBAP Sigma-Aldrich) in $1.0 \cdot 10^{-3}$ mol L^{-1} as a supporting electrolyte. The electrochemical cell was equipped with a glassy carbon (A = 3 mm^{2}) working electrode, a platinum foil auxiliary electrode and Ag/AgCl as the reference electrode in a Luggin capillary probe. Voltammograms were performed at a scan rate of 50–2000 V s^{-1}, with complex concentrations of 1 mM. The ferrocenium/ferrocene redox couple was used as an internal reference ($E_{1/2}$ = 0.46 V *vs* Ag/AgCl).

2.5. Synthesis of complexes 1–4

Synthesis of [(*η*^{6}-*p*-cymene)RuCl$_2$(apy)] (**1**). Complex **1** was synthesized according to the literature method [40]. A solution of the precursor (100 mg, 0.16 mmol) with an excess of 2-aminopyridine (76 mg, 0.82 mmol) in toluene (10 mL) was stirred for 12 h at room temperature. The orange solid that precipitated was filtered off, washed with diethyl ether and dried under vacuum. Yield: 82 mg, 63%. Elemental analysis (%) calcd. for $C_{15}H_{20}Cl_2N_2Ru$ (400.34 g mol^{-1}): C, 45.01; H, 5.04; N, 7.00. Found (%): C, 44.92; H, 5.17; N, 6.70. Its identity was established by agreement of the ^{1}H NMR and IR with the original report. ^{1}H NMR: (see Table 2). ^{13}C (400 MHz, $CDCl_3$, *δ* ppm): 18.21 (C^{a}); 22.27 (C^{g}); 30.49 (C^{f}); 81.70 (C^{c}); 82.97 (C^{d}); 97.75 (C^{b}); 103.05 (C^{e}); 112.21 (C^{k}); 114.04 (C^{i}); 138.47 (C^{j}); 152.24 (C^{h}); 162.59 (C^{l}). (FTIR, cm^{-1}): 3372 and 3290 $\nu_{asN\text{-}H}$ (w); 3040 $\nu^{2}_{asCsp\text{-}H}$ (w); 2966 and 2863 $\nu^{3}_{asCsp\text{-}H}$ (w); 1594 $\nu_{asC=N}$ (s); 1611, 1469 and 1438 $\nu_{asC=C}$ (s); 1251 $\nu_{C\text{-}H}$ (w); 1061 ν_{as}C (w); 753 $\delta_{C\text{-}H}$ (s). UV–vis. (CH_3CN, Max nm): 419 (420 mol^{-1} L cm^{-1}), 292 (5600 mol^{-1} L cm^{-1}), 233 (9200 mol^{-1} L cm^{-1}).

Synthesis of [(*η*^{6}-*p*-cymene)RuCl$_2$(meapy)] (**2**). A solution of the precursor (200 mg, 0.32 mmol) with an excess of 2-methylaminopyridine (173 mg, 1.60 mmol) in toluene (10 mL) was stirred for 4 h at room temperature. The orange solid that precipitated was filtered off, washed with diethyl ether and dried under vacuum. Yield: 238.7 mg, 88.5%. An analytical sample was obtained by vapour diffusion of diethyl ether into a concentrated $CHCl_3$ solution at RT (with some occluded $CHCl_3$). Elemental analysis (%) calcd. for $C_{16}H_{22}Cl_2N_2Ru \cdot 0.17CHCl_3$ (414.32 g mol^{-1}): C, 44.68; H, 5.14; N, 6.45. Found (%): C, 44.25; H, 5.09; N, 6.64. Removal of residual $CHCl_3$ was achieved by redissolving and precipitating with diethyl ether. Final purity was monitored by very careful NMR measurements showing the absence of C or H containing impurities. ^{1}H NMR: (see Table 2). ^{13}C (400 MHz, $CDCl_3$, *δ* ppm): 18.14 (C^{a}); 22.50 (C^{g}); 30.12 (C^{f}); 30.51 (C^{m}); 82.07 (C^{c}); 82.74 (C^{d}); 97.34 (C^{b}); 103.47 (C^{e}); 108.81 (C^{k}); 113.28 (C^{i}); 138.99 (C^{j}); 153.62 (C^{h}); 163.13 (C^{l}). (FTIR, cm^{-1}): 3259 $\nu_{asN\text{-}H}$ (w); 3051 $\nu^{2}_{asCsp\text{-}H}$ (w); 2953 and 2870 $\nu^{3}_{asCsp\text{-}H}$ (w); 1573 $\nu_{asC=N}$ (s); 1615, 1473 and 1429 $\nu_{asC=C}$ (s); 1259 $\nu_{C\text{-}H}$ (w); 1073 ν_{as}C (w); 853 $\delta_{C\text{-}H}$ (s), 749 $\delta_{C\text{-}H}$ (s). UV–vis. (CH_3CN, Max nm): 419 (800 mol^{-1} L cm^{-1}), 305 (5400 mol^{-1} L cm^{-1}), 242 (22000 mol^{-1} L cm^{-1}).

Synthesis of [(*η*^{6}-*p*-cymene)RuCl$_2$(bzapy)] (**3**). Complex **3** was synthesized according to the literature method [40]. A solution of the precursor (200 mg, 0.32 mmol) with an excess of 2-benzylaminopyridine (300 mg, 1.60 mmol) in toluene (10 mL) was stirred for 4 h at room temperature. The orange solid that precipitated was filtered off, washed with diethyl ether and dried under vacuum. Yield: 237.4 mg (74.3%). Elemental analysis (%) calcd. for $C_{15}H_{20}Cl_2N_2Ru$ (400.34 g mol^{-1}): C, 53.88; H, 5.34; N, 5.71. Found (%): C, 53.62; H, 5.37; N, 6.75. It proved impossible to obtain this complex in pure crystalline form and crystals suitable for X-ray diffraction could not be obtained. To obtain pure material, it was repeatedly dissolved and re-precipitated as an amorphous solid with ether, followed by vacuum drying. Finally, the identity and purity could be confirmed by very careful ^{1}H NMR analysis. ^{1}H NMR (see Table 2). ^{13}C (400 MHz, $CDCl_3$, *δ* ppm): 19.49 (C^{a}); 23.67 (C^{g}); 31.91 (C^{f}); 49.12 (C^{m}); 83.43 (C^{c}); 84.10 (C^{d}); 98.91 (C^{b}); 104.84 (C^{e}); 109.08 (C^{k}); 115.06 (C^{i}); 128.99 (C^{p}); 130.39 (C^{o}); 138.84 (C^{n}); 140.38 (C^{j}); 154.96 (C^{h}); 163.22 (C^{l}). (FTIR, cm^{-1}): 3238 $\nu_{asN\text{-}H}$ (w); 3046 $\nu^{2}_{asCsp\text{-}H}$ (w); 2953 and 2860 $\nu^{3}_{asCsp\text{-}H}$ (w); 1573 $\nu_{asC=N}$ (s); 1618, 1475 and 1434 $\nu_{asC=C}$ (s); 1237 $\nu_{C\text{-}H}$ (w); 1067 ν_{as}C (w); 843 $\delta_{C\text{-}H}$ (s), 763 and 703 $\delta_{C\text{-}H}$ (s). UV–vis. (CH_3CN, Max nm): 420 (600 mol^{-1} L cm^{-1}), 305 (4400 mol^{-1} L cm^{-1}), 242 (17200 mol^{-1} L cm^{-1}).

Synthesis of [(*η*^{6}-*p*-cymene)RuCl$_2$(py)] (**4**). The complex **4** was synthesized according to the previously reported method [41,42]. A solution of the precursor (100 mg, 0.16 mmol) with an excess of pyridine (30 mg, 0.37 mmol) in toluene (5 mL) was stirred for 4 h at room temperature. The orange solid that precipitated was filtered off, washed with diethyl ether and dried under vacuum. Yield: 108.5 mg (80.2%). Elemental analysis (%) calcd. for $C_{15}H_{20}Cl_2N_2Ru$ (400.34 g mol^{-1}): C, 46.76; H, 4.97; N, 3.64. Found (%): C, 46.75; H, 4.74; N, 3.94. Its identity and purity were established by agreement of the ^{1}H NMR data with ref [40]. ^{1}H NMR (see Table 2). ^{13}C (400 MHz, $CDCl_3$, *δ* ppm): 19.61 (C^{a}); 23.71 (C^{g}); 32.08 (C^{f}); 83.68 (C^{c}); 84.26 (C^{d}); 95.51 (C^{b}); 104.99 (C^{e}); 125.94 (C^{i}); 138.97 (C^{j}); 156.36 (C^{h}). (FTIR, cm^{-1}): 3046 $\nu^{2}_{asCsp\text{-}H}$ (w); 2963 and 2852 $\nu^{3}_{asCsp\text{-}H}$ (w); 1531 $\nu_{asC=N}$ (s); 1600, 1468 and 1437 $\nu_{asC=C}$ (s); 1210 $\nu_{C\text{-}H}$ (w); 1067 ν_{as}C (w); 881 $\delta_{C\text{-}H}$ (s). UV–vis. (CH_3CN, Max nm): 408 (720 mol^{-1} L cm^{-1}), 244 (28200 mol^{-1} L cm^{-1}).

2.6. *DNA interaction studies*

All measurements with *calf-thymus deoxyribonucleic acid* (CT-DNA) were taken in a PBS buffer (NaCl 0.137 mol; KCl $2.68 \cdot 10^{-3}$ mol; KH_2PO_4 $1.47 \cdot 10^{-3}$ mol; Na_2HPO_4 0.016 mol; *p*H 7.6). The CT-DNA concentration per nucleotide was determined by absorption spectrophotometric analysis using a molar absorption coefficient of 6600 mol^{-1} L cm^{-1} at 260 nm [43]. The spectroscopic titrations were carried out by adding increasing amounts of CT-DNA to a solution of the complex in a quartz cell and recording the UV–vis spectrum after each addition. The binding affinities (K_b) were obtained by using the Benesi-Hildebrand equation: $[DNA]/(\varepsilon_a\text{-}\varepsilon_f) = [DNA]/(\varepsilon_b\text{-}\varepsilon_f) + 1/[K_b(\varepsilon_b\text{-}\varepsilon_f)]$ [44], where ε_a is the apparent molar absorptivity, which corresponds to the ratio between an absorption of the measurement and a concentration of the complex ($A_{observed}$ [complex]); ε_f is molar absorptivity of the free complex (without addition of DNA); ε_b is molar absorptivity of the DNA-bound complex; K_b is the binding constant. Plotting a graph of $[DNA]/(\varepsilon_a - \varepsilon_f)$ *versus* [DNA] gives the ratio of the angular and linear coefficients of intrinsic binding (K_b) between the complex and DNA.

Ru-complex/CT-DNA solution viscosities at different concentration ratios were measured using a Lovis 2000 M/ME Rolling-Ball Viscometer maintained at 25 °C in a constant temperature bath. Aqueous solutions of CT-DNA were studied by viscosity measurements at ambient pressure. The DNA concentration was fixed at 20 μmol L^{-1}, and flow time was measured with a digital stopwatch. The mean values of three measurements were used to evaluate the viscosity η of the samples. Specific viscosity was plotted as a function of DNA and Ru-complex concentrations. The values for relative specific viscosity $(\eta/\eta_0)^{1/3}$, where η_0 and η are the specific viscosity contributions of DNA in the absence (η_0) and in the presence of the complex (η), were plotted against [complex]/[DNA] [45].

Circular dichroism spectra were measured on a Jasco J-810 spectropolarimeter equipped with a Peltier temperature control unit held at 25 °C (Jasco Corp. Tokyo, Japan). CT-DNA and Ru-complexes were measured alone or at different mixture concentrations in PBS (*p*H 7.6) in a 1 mm path length quartz cell between 220 and 340 nm at a scanning speed of 100 nm min^{-1} and by the averaging of 10 scans. The absence of CD signal for Ru-complexes (200 μmol L^{-1}) was verified. Modification of the mixture signal was monitored after addition of Ru-complexes solutions to a fixed concentration of CT-DNA solution in two ratios [DNA] [Ru-Complex] 1:1 and 1:2.

Interaction of Ru-complexes with DNA was studied by ethidium bromide (EtBr) competition assays. All measurements were performed on a Varian Cary Eclipse Fluorescence Spectrophotometer using a 1 cm pathlength cuvette. These competition experiments were carried out in PBS (pH 7.6), by keeping the molar ratio of DNA (nucleotide) to EtBr (5:1) constant and varying the Ru-complex concentrations (0–420 μmol L^{-1}). The excitation wavelength was 530 nm, and the emission range was set between 550 and 700 nm for all bromide fluorescence measurements.

2.7. BSA interaction studies

Circular dichroism spectra of *bovine serum albumin* (BSA) were recorded using a Jasco J-720 Spectropolarimeter at 25 °C The measurements in presence and absence of the complexes were made in the range of 203–260 nm using a 0.1 cm cell with ten scans averaged for each CD spectra. The BSA concentration was maintained at 2.5 μmol L^{-1}, and the molar ratio of complexes to BSA concentration was 1:2, 1:1 and 10:1. The thermal denaturation experiments were performed over 15–95 °C, with intensity measurements taken at 208 and 222 nm, every 5C°. Melting temperatures were calculated with sigmoidal fit employing the software Origin (Microcal).

2.8. Cell culture and cytotoxicity assays

In vitro cytotoxicity assays on cultured human tumor cell lines still represent the standard method for initial screening of antitumor agents. The complexes were assayed against human cell lines: cervical carcinoma HeLa (ATCC® CCL-2™), the complexes **1** and **2** were assayed against human laryngeal carcinoma HEp-2 (ATCC CCL-23) and the complex **1** against the murine melanoma B16F10 (ATCC® CCL-6475™) and Vero Cell (ATCC CCL-81) derived from the kidney of an African green monkey. The cells were routinely maintained with Iscove's Modified Dulbecco's medium, supplemented with 10% fetal bovine serum (FBS), at 37 °C in a humidified 5% CO_2 atm. For the cytotoxicity assay, 5×10^5 cells·mL^{-1} were seeded in 200 μL of complete medium in 96-well plates. Stock solutions were prepared by dissolving the complexes in dimethyl sulfoxide (DMSO) followed by dilution with PBS, and serial dilutions of these stock solutions were made using culture media. In this way the lowest possible DMSO concentration was used in these experiments. The cells were exposed to the complex in different concentrations for a 24 and 48 h period. However, it was necessary to deviate from the standard MTT test protocol because of the sensitivity of **1** to **4** to ligand displacement by DMSO (see below). In this modified protocol, the stock solutions were prepared by dissolving the complexes in PBS buffer. The viability of cultured cells for these protocols described above was evaluated using MTT (3-(4,5-dimethylthiazol-2-yl)-2,5-diphenyltetrazolium bromide) assays [46]. In this method, the MTT conversion to formazan by metabolically viable cells was monitored by SpectraMax 190 Microplate Reader (Molecular Devices) at 540 nm. Cell survival rate (%) *versus* drug concentration (logarithmic scale) was plotted to determine the IC_{50} (drug concentration at which 50% of the cells are viable relative to the control), with its estimated error derived from the average of 3 trials.

3. Results and discussion

3.1. Synthesis and characterization of Ruthenium(II)-arene complex

The synthesis of the series of [(η^6-*p*-cymene)$RuCl_2$L] complexes (Scheme 1) was achieved via bridge cleavage of [{(*p*-cymene)Ru(μ-Cl)Cl}$_2$] with a 5:1 ratio of ligands L (**apy**, **meapy** and **bzapy**) in toluene at RT for **1**–**3**. Complex **4** required a 2.3:1 mol ratio of **py** in toluene at reflux to achieve complete reaction. The complexes were

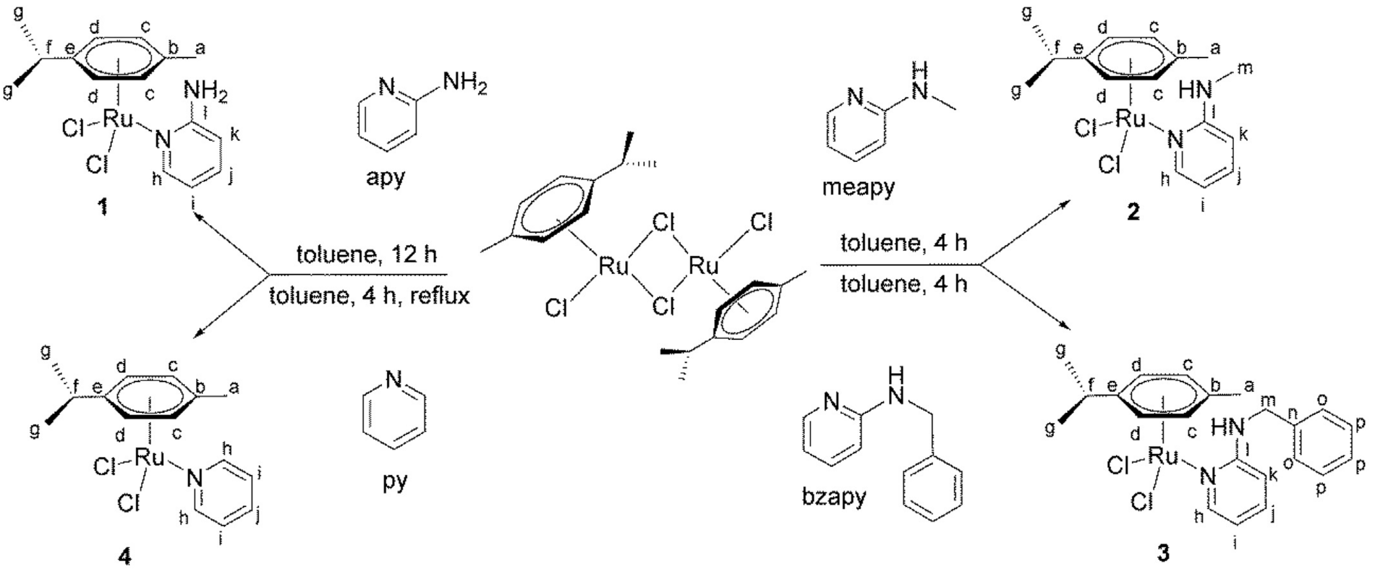

Scheme 1. Synthesis and structures of complexes **1**–**4**.

Table 1
Molar conductance data for the series of complexes [(η^6-*p*-cymene)RuCl$_2$L].

Complex	Λ_m CH$_3$CN (μS·cm^{-1}) 0 h [a]	Λ_m CH$_3$CN (μS·cm^{-1}) 24 h [a]	Λ_m H$_2$O (μS·cm^{-1}) [b]
1	33.4	35.5	___
2	33.3	35.1	69.8
3	31.4	32.6	___
4	35.6	36.8	___

[a] CH$_3$CN $1 \cdot 10^{-3}$ mol L^{-1}.
[b] H$_2$O $1 \cdot 10^{-3}$ mol L^{-1}.

Table 2
Potential data for complexes **1**–**4**.

Complex	E^{I}_{pa}/V	E^{II}_{pa}/V	E^{III}_{pa}/V	E^{III}_{pc}/V	$E^{III}_{1/2}$/V^a	ΔE_p ^{III}/V^b	I_{pc}/I^{IIIc}_{pa}	E^{IV}_{pc}/V	E^{V}_{pc}/V	E_{window}/V^d
1	1.37	1.41	1.52	1.43	1.47	0.09	0.11	−0.91	−1.22	2.28
2	1.15	1.23	1.42	1.33	1.37	0.09	0.20	−0.98	−1.30	2.13
3	1.22	1.32	1.49	1.40	1.44	0.09	0.15	−0.92	−1.22	2.14
4	1.16		1.39	1.33	1.36	0.06	0.04	−1.04	−1.32	2.20

[a] $E_{1/2} = (E_{pa} + E_{pc})/2$.
[b] Measured by difference between E_{pa} and E_{pc}
[c] Evaluated as by Ref. [55] (to 2 V s^{-1}).
[d] Measured by difference between E^{I}_{pa} and E^{IV}_{pc}.

prepared as orange solids, stable to light and in air, with yields ranging from 63 to 88%. In addition, all the complexes are soluble in water, halogenated solvents and polar organic solvents such as DMSO, dichloromethane and acetonitrile, but insoluble in diethyl ether (see Figs. S11–S14). The molar conductance of CH$_3$CN solutions of **1**–**4** were measured ($1.00 \cdot 10^{-3}$ M) after mixing and after 24 h to determine if solvolysis was a factor for the voltammetric and electronic spectroscopic experiments. The results are convincingly attributable to non-electrolyte solutions with no change after 24 h within experimental error (Table 1) [36]. In addition, conductivity measurements on aqueous solutions of **2** were performed ($1.00 \cdot 10^{-3}$ M) to confirm the labilization of the chloride ligand and the results suggest that partial hydrolysis occurs rapidly.

3.2. Molecular structures by X-ray crystallography and DFT computation

Single-crystal structures on **1** and **4** have previously been reported were deposited in the Cambridge Structural Database, version 5.38, Nov 2016 (CSD) [47] under CSD refcodes: JOBCOS [39] for **1** and MIXSOD [41] and MIXSOD01 [13] for **4**, respectively. For complex **3**, a structure of a closely related complex exists in which **bzapy** is coordinated in [(η^6-ethylbenzoate)RuCl$_2$L] (**3b**), CSD refcode: OHICAL [48]. In this work, we report the new crystal structure of the 2-methylaminopyridine complex **2** (see Table S1, Fig. S1 in the *Supplementary Information* (SI) for structure details). The derived interatomic parameters of these four structures in their crystalline lattices are compared to those from UB3LYP//6-31 + G(d), SPK-DZCD hybrid DFT calculations (Table S2, Fig. S2) on **2** and more extensively on **1** as a representative electronic model system. The crystal structure of **2** displayed considerable complexity, containing CHCl$_3$ solvent of crystallization, two independent molecules in the asymmetric unit and a wholesale disorder of the **meapy** ligands (only the major components of the disorder are shown in Fig. 1). In each case, there are hydrogen bonds from the ligand N–H to metal-bound chloride ligands. Note that in the Ru1 molecule for the major (75% refined occupancy) component, the CH$_3$NH group (N2) is oriented towards the end of the cymene ligand bearing the isopropyl group (Cl1), whereas in the Ru2 molecule in the major (63% refined occupancy) component, the equivalent group (N4) is oriented towards the methyl group side of the cymene ligand (Cl3). The minor components of each disordered pair have the **meapy** groups flipped towards the opposite ends of the respective cymene ligands. The same disorder was observed for crystals grown solvent-free from diethyl ether and chlorobenzene; apparently the molecular volume of **meapy** and *para*-cymene are extremely similar.

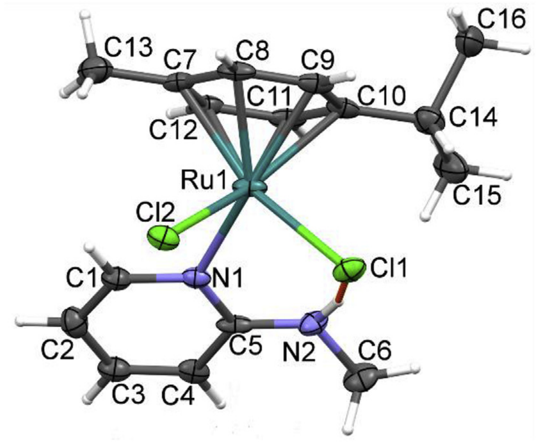

Fig. 1. Displacement ellipsoids (50% probability) plot of one of two similar independent molecular structures of **2** as found in the crystal lattice, with the atom numbering scheme. Only the major components of the **meapy** disorder models are shown. The H-bond geometry is indicated by a dashed orange line (see Table 1). (For interpretation of the references to colour in this figure legend, the reader is referred to the Web version of this article.)

All four molecules adopt very similar molecular structures to that of **2** in their crystal lattices (see Fig. S1 in the Supporting Information). Key features are the classic "piano-stool" architecture wherein the η^6-arene groups fill three facial sites in the *pseudo*-octahedral geometry at ruthenium. In each case, including **4**, the coordinated pyridine ring is oriented approximately parallel to that of the η^6-arene albeit angled downwards by ~30°. Consideration of space filling models (Fig. S3) indicates that this conformation represents a rotational minimum due to constraints between the ortho hydrogen atoms in pyridine with Cl1,2. This conformational preference is augmented by N2H2···Cl1 hydrogen bonding in **1** − **3b**, which is retained in gas-phase DFT calculated structures. Notably, the pyridyl ligands are all κ^1 coordinated through N1 in these [(η^6-*p*-cymene)RuCl$_2$L] complexes, whereas the κ^2-*N*,*N′*-chelating geometry is known in (2-aminopyridine)-dichloro-bis(triphenylphosphine)-ruthenium(II), CSD refcode: IHIWAX (Fig. S4) [49]. Thus, despite the 2-NHR substitution in **1**–**3**, all complexes are confirmed to be of type A (see the Introduction). Interestingly, a recent paper reports on several [(η^6-*p*-cymene)RuCl$_2$(2-halogenated-5-aminopyridines)] with unexpected coordination from the *amino* group rather than the more basic ring N [50].

3.3. Solid state structural features from FT-IR and Raman spectra

The FT-IR spectra (Fig. S5 and Table S3) contain the expected bands for the pyridine ligands in addition to those of the η^6-*p*-cymene and chloride ligands but have low diagnostic information save for the $\nu_{as(N-H)}$ bands in **1**–**3** (and their absence in **4**). The observed stretching frequencies follow the inter- and intramolecular N···Cl hydrogen bonding distances from respective crystal structures of 3.234 ($\nu_{1(N-H)} = 3390\ cm^{-1}$) and 3.243 Å ($\nu_{2(N-H)} = 3372\ cm^{-1}$) in **1**, and with intramolecular distances 3.165 Å in **2** ($\nu_{(N-H)} = 3259\ cm^{-1}$) and for **3** 3.147 Å in OHICAL ($\nu_{(N-H)} = 3238\ cm^{-1}$). The correlation of N–H···Cl distances with N–H stretching frequencies is long known from the literature [51]. The Raman spectra (Fig. S6, Table S4) corroborate the FT-IR results.

3.4. Solution structures as established by NMR

A full assignment of the solution-phase ^{1}H and ^{13}C NMR signals was achieved on the basis of 1D (NMR) and 2D experiments (Table S5 and Scheme S1, along with full archival spectra in Figs. S7–9). These data, especially the ^{1}H spectra, provide convincing information about the solution structures and the purities of **1**–**4**, showing that (i) the *p*-cymene ring is rotationally fluxional, rendering an effective C_{2v} symmetry despite coordination to the ruthenium and (ii) the **apy**, **meapy** and **bzapy** ligands retain similar geometries in solution in $CDCl_3$ as deduced from the solid-state structures (see above). Thus, whilst the NH_2 signal in **1** integrates to 2H, it has a chemical shift ($\delta = 6.16$) intermediate between that of hydrogen-bonded and non-hydrogen-bonded NH. By contrast, the single NH proton signals of **2** ($\delta = 7.28$) and **3** ($\delta = 8.10$) are deshielded. This data is consistent with the intermolecular H-bonding strengths **3** > **2** > **1** also shown by crystallographic *d*(N···Cl) data and the trend of the $\nu_{as(N-H)}$ bands in the FTIR spectra. The other ^{1}H chemical shifts correlate well with the expected substituent effects from the presence of the 2-amino groups on pyridine in **1**–**3** and its absence in **4**. The δ and the $\Delta\delta$ values for *p*-cymene ring protons $H_{2,3}$ are remarkably invariant for the series and quite similar to those in the chloride-bridged precursor complex (*pseudo*-AB doublets at 5.37 and 5.51 ppm, and $^3J_{HH} = 6.04$ Hz). The observation of $^3J(H^n,H^m) = 5.0$ and 5.5 Hz in spectra of **2** and **3** in $CHCl_3$ solution indicates lack of exchange of the NH signals. This is also consistent with a dominant H-bonded conformation in solution. This coupling is confirmed by gCOSY experiments (see Fig. S9 in the SI).

3.5. Electronic structure from DFT calculations on 1 as a model system

The electronic structure of complex **1** was examined in detail using hybrid DFT calculations at the UB3LYP//6-31 + G(d),SPK-DZCD level of theory. The neutral molecule was geometry optimized both in the gas phase and in an aqueous solvent model. In addition, the oxidation states −2, −1, +1 and + 2 were all optimized (see Fig. S10 in the SI). The need for computation was indicated to assist with assignment of the electronic absorption spectra and particularly the rather odd voltammetric behavior of the complexes (see below). All complexes optimized to a reasonable geometry with the strongest bonding between the *p*-cymene and metal in the neutral (18*e*) state, as expected (*p*-cymene ring centroid to Ru distance of 1.766 Å). Both oxidized and reduced forms have weaker bonding and the anions optimize with one chloride ligand migrating from Ru to sites that only hydrogen-bond to the NH group. In the 20*e* dianion, the arene converts to η^4–coordination, fully consistent with classical organometallic bonding models. All charge states display NH···Cl H-bonding, either to coordinated or displaced halides (see Fig. S10). The following discussion deals specifically with neutral **1** in the gas-phase model.

The calculated electronic structure presented in Fig. 2 (left) indicates that the highest occupied orbitals (HOMO, HOMO-1, HOMO-2, corresponding closely to the t_{2g} set of the *pseudo*-octahedral geometry) have mixed Ru 3*d* orbitals and Cl 2*p*-π* character along with minor participation from C 2*p* orbitals of the *p*-cymene ring. These three frontier molecular orbitals (FMO) are almost degenerate and lying only slightly lower in energy are two (accidentally) degenerate levels: HOMO-3, with mostly non-interacting Cl p_z character, and HOMO-4, the essentially unperturbed aminopyridine filled π3 level. In turn, the two lowest unoccupied orbitals (LUMO and LUMO+1, corresponding to the e_g set) have both Ru 3*d* and significant Ru–Cl σ* character. Above these, LUMO+2 is an almost unperturbed pyridine π4 MO [52].

3.6. Electrochemical characterization in solution by voltammetry

The redox behavior of **1**–**4** was investigated by cyclic voltammetry (CV). The CVs of **1**–**4**, recorded at a glassy carbon electrode in 0.1 M TBAP/CH_3CN solutions as the supporting electrolyte (*vs.* Ag/AgCl), are shown in Fig. 3 and the pertinent data are presented in Table 2 (see also Figs. S11–S16 in the SI). Most importantly, and the goal of the voltammetric study undertaken for this project, is the evidence for a very wide redox stability window ($E_{window} = 2.2$ V),

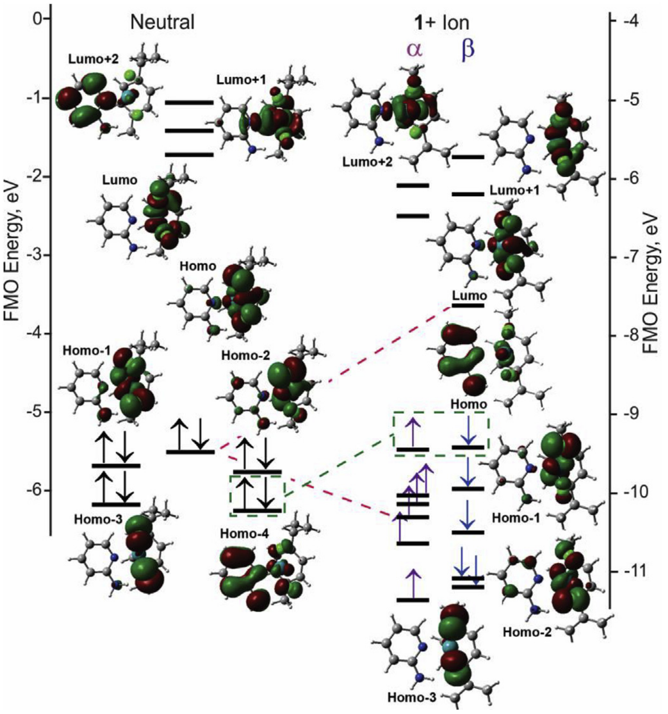

Fig. 2. Frontier molecular orbitals (FMO) and energy levels from gas phase DFT calculations on complex **1** (singlet state, left) and **1**$^+$ (doublet state, right; for clarity only the β-spin orbitals in **1**$^+$ are shown). The energy scale at right is displaced upwards by about 4 eV.

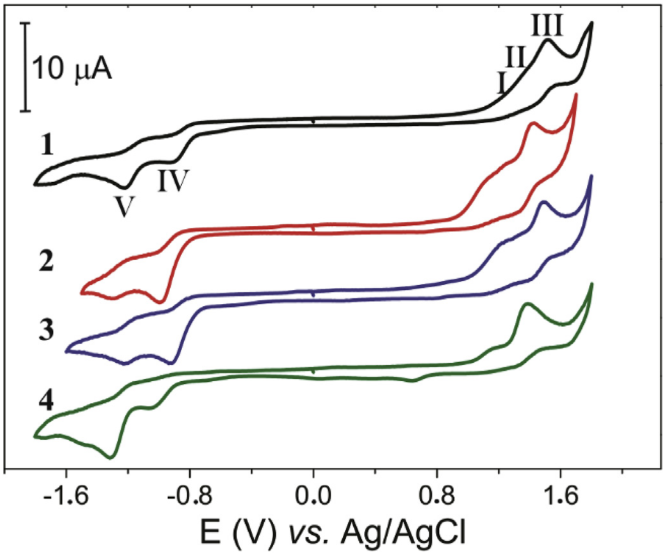

Fig. 3. Cyclic voltammograms of **1**–**4** at $2.0 \cdot 10^{-3}$ mol L^{-1} in TBAP/ACN 0.1 mol L^{-1} *vs.* Ag/AgCl; obtained at 100 mV s^{-1}.

defined by the difference between E^{I}_{pa} and E^{IV}_{pc}, extending far out in both the anodic and cathodic regions. This provides direct evidence for the oft-claimed stabilization of the Ru(II) oxidation state by η^6-arene ligands [9]. This stability is only marginally affected, compared to **py** in **4**, by amino-substitution in **1**–**3**. Importantly, this range is much wider than the physiological E° range, between ~−1 V and +1 V *vs.* SHE, so this class of complex can be expected to remain as Ru(II) in vivo so long as the arene ligand remains attached [53].

The detailed CV behaviour of **2**, representative of the 2-aminpyridine complexes, was studied first in the anodic region at a scan rate of 100 mV s^{-1}, whereby it exhibits two very closely-spaced chemically irreversible processes at around 1.15 and 1.23 V, designated I and II, respectively, followed by process III at E_{pa} 1.37 V, for which a small return wave can be detected. These processes could *in principle* correspond to a possible sequence of one-electron oxidations $[(\eta^6\text{-}p\text{-cymene})RuCl_2(\mathbf{meapy})]^{0/+/2+/3+}$, but such closely spaced waves would be quite unusual for an isolated metal complex due to the effects of charge buildup.

Further insight into these oxidation processes is provided by the computed electronic structure of the 1 + state. After removal of the first electron from a Ru(*d*)-Cl(*p*-π) orbital (the HOMO at left in Fig. 2), significant orbital re-organization occurs. The result is that the HOMO of the doublet state ion derives from the filled amino-pyridine ligand π3 level (which is HOMO-4 of the neutral state.) The unpaired electron retains Ru(*d*) character at lower energy (it is the α spin orbital that has a very similar topology to the β LUMO shown on the diagram; *the energy evolution is shown in dashed red lines on* Fig. 2). Because the aminopyridine π orbitals are non-interacting with the metal, they do not experience the same amount of energy-lowering in the cationic state as the metal orbitals do. This suggests the possibility that second (and third) electrons in oxidation processes II (and III) come from the ligand and the metal remains Ru(III) in all these oxidized states. In short, aminopyridine ligands appear to function as redox-non-innocent ligands *in the oxidized cationic states* [54].

In the cathodic region, two irreversible reduction peaks are observed (processes IV and V, E^{IV}_{pc} at −0.98 and E^{V}_{pc} at −1.30 V, respectively). These processes can be confidently attributed to sequential occupation of the LUMO of the neutral complex (Fig. 2). Although formally this involves Ru^{II}/Ru^{I} reduction, this orbital also has significant Ru—Cl σ* character. In this regard, it is interesting to observe that DFT calculations optimize to geometries where one of the Cl^- ions leaves the metal and attaches remotely to the NH moiety via H-bonding (see Fig. S10 in the SI). Ligand dissociation could thus be responsible for the (chemical) irreversibility of these processes.

The CVs of all four complexes were also recorded upon scanning from +1.0 to +1.9 V and from −0.6 to −1.7 V over $v = 50\text{–}2000$ mV s^{-1} (see Figs. S13–S16 in the SI). In all cases, the linearity of I_p *vs.* $v^{1/2}$ plots demonstrates that mass transport of these compounds to the electrode surface is diffusion-controlled. The voltammetric features (I_{pa}/I_{pc} less than unity and ΔE_{peak} values about 90 mV) show that oxidation-reduction of these compounds is chemically and electrochemically almost reversible in fast scans and irreversible at lower scan rates.

3.7. Electronic absorption spectroscopy

Electronic absorption spectra of complexes **1**–**4** were acquired in the concentration 10^{-4} mol L^{-1}, in different solvents at RT, such as: acetonitrile, water and PBS buffer (Fig. 4). The spectra in all these solvents showed similar broad low-energy bands with maxima at 389–416 nm ($\varepsilon = 2100\text{-}800$ L mol^{-1} cm^{-1}), which can be attributed to LUMO←HOMO transitions. TD-DFT calculations, carried out in CH_3CN and water solvent models, indicate that several transitions involving the cluster of highest filled orbitals probably contribute to these bands which thus have significant *d*←*d* character (albeit with covalent contributions from Cl and pyridine N σ orbitals).

In addition, there are two sets of higher-energy bands. The first, with maxima close to 300 nm for **1**–**3**, are noticeably absent in the spectra of **4**. These bands may involve excitation from HOMO-4 to the LUMOs or from the higher filled orbitals to LUMO+2. Probably the 2-aminopyridine π orbitals are involved and are thus either LMCT or MLCT bands of modest intensity. Very intense bands at ~250 nm could include lower-lying metal electron excitation to high virtual orbitals; furthermore, *p*-cymene and pyridine π*←π transitions. The TD-DFT calculations indicate that most bands have multiple transition contributions with varying oscillator strengths.

A noticeable feature (see the insets in Fig. 4) is that the LUMO←HOMO bands are blue-shifted by 12–26 nm in the aqueous spectra. There is a strong expectation that these complexes will undergo hydrolysis either partly or completely in water (Scheme 2) [18,56–58]. Our conductivity data (Section 3.2) suggest that the hydrolysis is relatively slow and thus likely to stop at a single halide replacement. Replacement of one chloride ligand by water is consistent with lowering the highest occupied FMOs due to weaker π* character, and thus with a blue-shift. Since the hydrolyzed complexes will tend to be cationic (especially in the enhanced acidic environment of cancer cells), these processes have important implications for the *in vitro* biological test results (see below).

3.8. DNA interaction studies

Among organometallic ruthenium complexes, a range of compounds exhibit potent anticancer activity. Many cytotoxic agents were proven to have DNA as the cellular target. These molecules elicit a range of cellular responses which implies different mechanisms of action [5,7]. The interaction of drug molecules with DNA can be categorized using simple limiting models as shown schematically in Fig. 5 as non-covalent (intercalation, groove binding, electrostatic attraction) or covalent (condensation or hydrogen-bonding with nitrogen bases or condensation with phosphate of the DNA backbone).

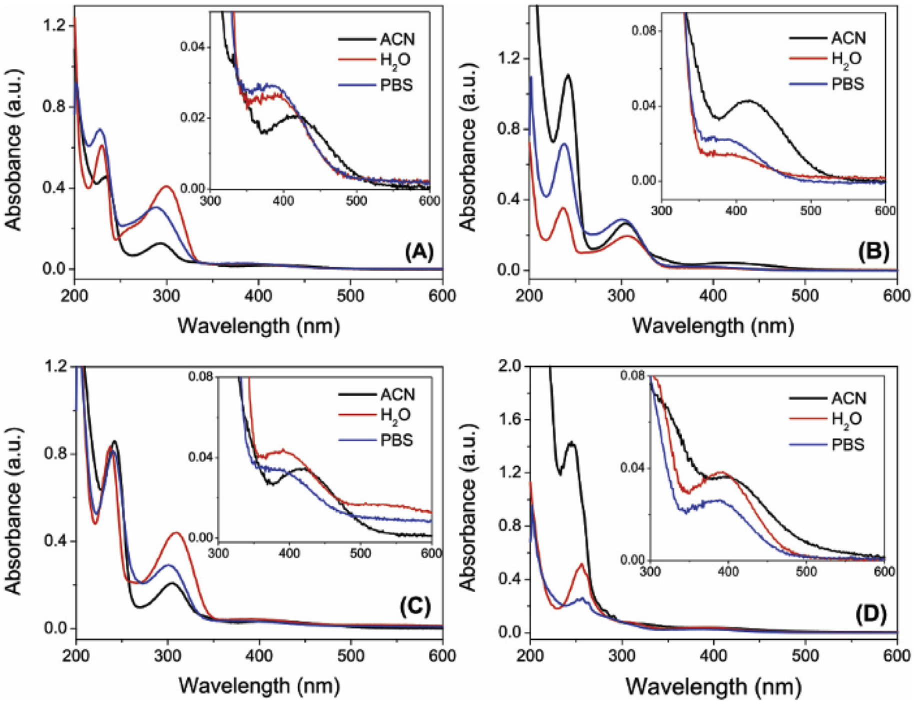

Fig. 4. UV–vis spectra of the series of complexes [(η^6-*p*-cymene)$RuCl_2L$] in acetonitrile, water and PBS buffer. In each case, the main window covers 200–600 nm, with an expanded inset from 300 to 600 nm. (A) Complex **1**. (B) Complex **2**. (C) Complex **3**. (D) Complex **4**. Tabulated data provided in Table S4.

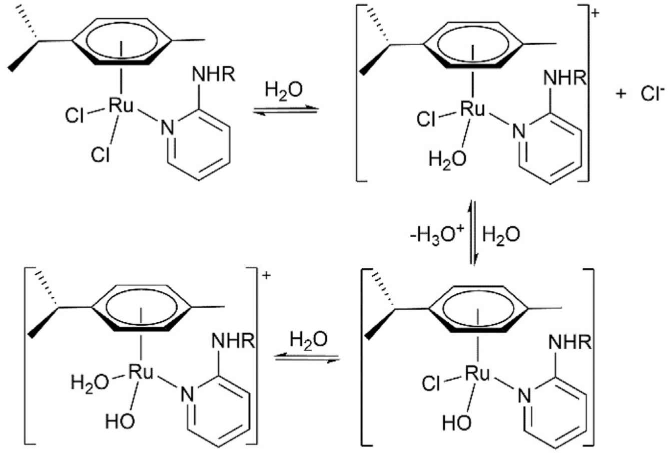

Scheme 2. Some of the equilibria connected to chloride hydrolysis in aqueous phases.

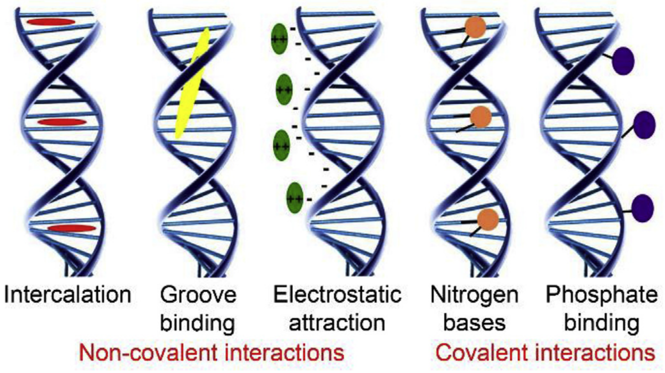

Fig. 5. Cartoons showing common modes of interaction between drug molecules and double-stranded DNA. Adapted from *Rev. Virtual Quim.*, **2015**, *7* (6), 1998–2016, with the permission of the Brazilian Chemical Society.

3.8.1. UV–vis spectroscopy

UV–vis absorption measurements have been successfully used to study the mode and magnitude of interaction of complexes **1**–**4** with CT-DNA. DNA–complex interactions are evidenced by this technique through changes in absorbance intensity and position of the absorption band. When complexes **1**–**4** were titrated with CT-DNA, hyperchromism (i.e. increased intensity) was observed, along with a small red-shift of 2–4 nm in the presence of complexes **2** and **3** (Fig. 6). The binding strengths of **1**–**4** were quantified from the values of intrinsic binding constant K_b, determined using the Benesi-Hildebrand equation (Table 3) [43]. Whereas hypochromism (i.e. decreased intensity) is indicative of DNA intercalation (due to contraction of the helix and conformational changes caused by changes in the π-π stacking interactions) [59], hyperchromism is attributed to electrostatic interaction between complexes and the negatively charged phosphate backbone at the periphery of the double helix CT-DNA or to secondary damage of the DNA double helix structure [60–63]. The presence of complexes **1** to **4** resulted in hyperchromism in DNA absorption spectra suggesting non-intercalative binding between DNA and the complexes. This is corroborated by the size of the intrinsic binding constants K_b being in the micromolar range [64].

3.8.2. Circular dichroism spectroscopy

The circular dichroism (CD) technique is responsive to changes in the chiral structure of DNA and is used to study variations in DNA conformation upon its interaction with small molecules [65]. B-form calf thymus DNA exhibits a negative band at 245 nm caused by helicity and a positive band with maximum at 275 nm caused by base stacking [66,67].

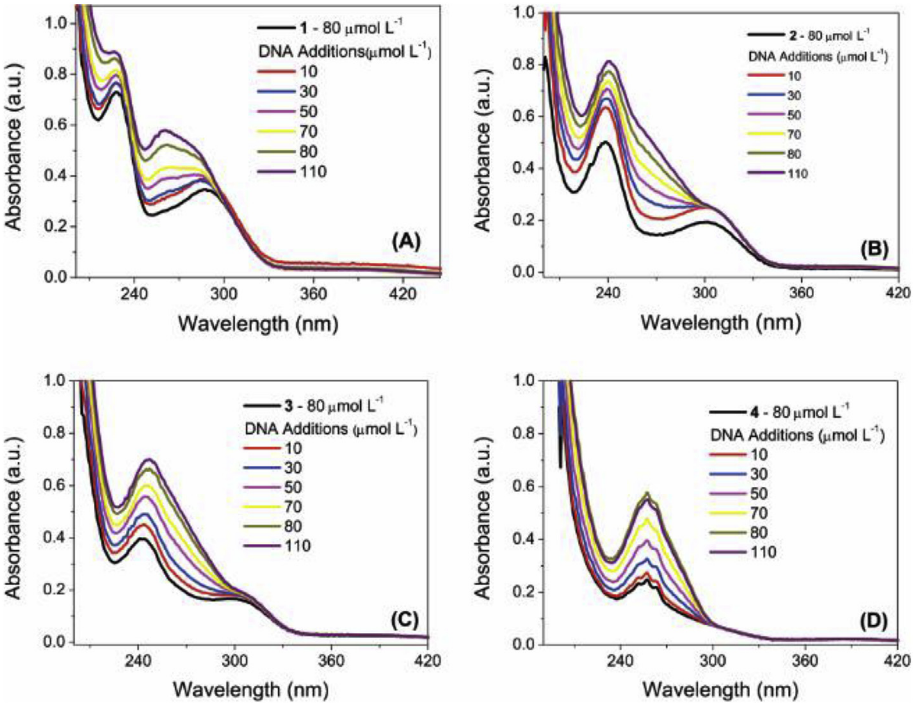

Fig. 6. Electronic spectra of the complexes in the absence and after successive additions of CT-DNA. (A) complex **1**; (B) complex **2**; (C) complex **3**; (D) complex **4**.

Table 3
Intrinsic binding constants (K_b) for interaction between CT-DNA and complexes **1**–**4**.

Complexes	Wavelength (nm)	K_b (M^{-1})
1	227	2.24×10^5
2	237	1.40×10^5
3	243	7.34×10^4
4	257	3.68×10^4

Distinct modes of interaction can be distinguished by changes in the spectra. Intercalation clearly enhances the signal intensity of both the base stacking and helicity bands, while groove binding and electrostatic interactions cause slight perturbations on positive and negative bands. In addition, changes just in the intensity, and not shape, of the observed CD results suggest a single binding mode. Changes in the shape of CD signals may indicate multiple ligand-DNA binding modes, changes in DNA conformation or ligand–ligand interactions [68].

To verify whether binding of the complex causes any conformational change of the DNA double helix, CD spectra of CT-DNA were recorded at different complex/CT-DNA ratios (Fig. 7, black lines). The addition of complexes **1**, **2** and **4** to CT-DNA slightly increased the intensity of the positive peak and decreased the intensity of the negative peak (Fig. 7). These changes in the CD spectra in the presence of the complexes indicate that complexes **1**, **2** and **4** interact with CT-DNA and stabilize the right-handed B-form of CT-DNA structure. These alterations in spectra are common in groove binding and electrostatic interactions [65].

3.8.3. *Ethidium bromide competition*

To confirm a non-intercalative binding mode, competition experiments with EtBr were performed. Classical intercalators displace EtBr from DNA bases, thereby decreasing its fluorescence emission [69]. Addition of complexes **1**–**4** to EtBr-DNA solutions does not alter emission intensity of EtBr by more than the dilution effect, which, together with the spectroscopic titration and CD results, indicates that these complexes are not DNA intercalators. (see Fig. 8).

3.8.4. *Viscosity measurements*

Hydrodynamic measurements are considered as unequivocal tests of DNA binding models in solution, clarifying the interaction mode of a compound with the nucleic acid. An interaction between the DNA double helix and a small molecule may cause length changes in DNA and as a result viscosity changes [44]. The values of relative specific viscosity $(\eta/\eta_0)^{1/3}$ were plotted against [DNA]/[complex] (Fig. 9). In this study, it was observed that increasing concentrations of complexes **1**–**4** do not significantly alter the DNA viscosity. Thus, it is possible to infer that these complexes are not covalent binders, and neither partial nor classical DNA intercalators.

3.9. *Cytotoxicity assays*

The cytotoxic effects were examined for the [(η^6-*p*-cymene)RuCl$_2$L] series complexes as well as for the ([(η^6–*p*-cymene)RuCl$_2$(DMSO)] obtained *in situ*, since ^{1}H NMR (see Fig. S18) tests performed for the complexes in the presence of DMSO demonstrate that there is a pyridine ligand lability with coordination by the DMSO molecule. The complexes thus formed by replacing monodentate pyridine ligands with DMSO were confirmed to also be neutral by conductivity tests (see Table S7). Coordination of DMSO in ruthenium pyridine complexes has been previously reported in the literature [18,70] and by comparison of data we can indicate that the DMSO is coordinated to the metal through sulfur [71,72].

The cytotoxic tests for [(η^6-*p*-cymene)RuCl$_2$L] complexes in DMSO were carried out against HeLa, Hep-2, B16F10 and Vero cells line (Table 4, Fig. S19), while tests carried in phosphate buffer were evaluated only against Hep-2 and B16F10 (Table 4, Fig. S20). Emphasis was placed on testing against the resistive HeLa line. The results obtained using an MTT assay showed that only **2** with DMSO achieved an IC$_{50}$ against the HeLa tumor line after a 24 h with IC$_{50}$ = 346 μmol L^{-1}. The *absence* of toxicity in aqueous solution suggests that the toxicity is due to the liberated **meapy**

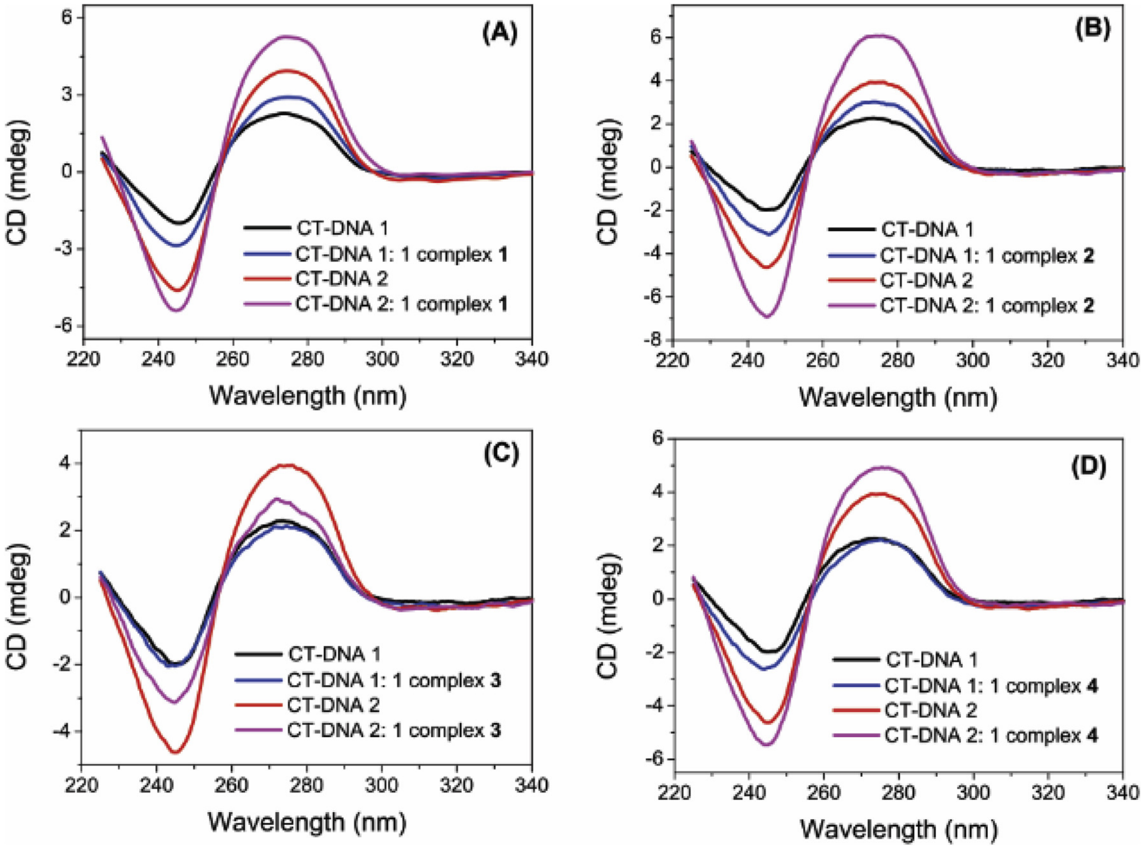

Fig. 7. CD spectra for CT-DNA (100 and 200 μmol L^{-1}) in PBS buffer (pH 7.6), with addition of 200 μmol L^{-1} of the complexes. (A) complex **1**; (B) complex **2**; (C) complex **3** and (D) complex **4**.

ligand. For the other complexes of the series with or without DMSO as well as for other tumor lines, HEp-2 and B16F10, it was not possible to determine IC$_{50}$ values in the range of concentrations investigated.

The low activity of [(η^6-*p*-cymene)RuCl$_2$L] series **1**–**4** against cancer cell lines is similar to results reported on a range of other type A complexes with simple substituted pyridines [10,12,14,16,18,28,73,74]. By contrast, the substituted aminopyridines reported by Richter et al. [27], bearing 4-carboxylatophenyl substituents at the amine, were shown to be more active against 8500C, MCF-7, SW-480 and 518A2 cancer cell lines, although only marginally more than the direct use of the corresponding substituted amino-pyridines in control tests [75].

3.10. BSA interactions

An important feature of biologically active compounds is their binding to proteins. The ability to interact with proteins affects the activity of a molecule in biological systems, so protein-binding studies are carried out to reveal the potential of new drug molecules. Bovine serum albumin protein is frequently used in these protein-binding studies because of its structural homology with human serum albumin (HSA). In order to characterize binding of complexes **1**–**4** to BSA, we carried out circular dichroism studies. The protein conformation was not significantly altered in the presence of complexes **1**–**4** (Fig. S17 in the SI). We further investigated the thermal stability of BSA in the presence of complexes **1**–**4**. When bound to a protein, small molecules tend to enhance the thermal stability, resulting in increased melting temperatures (*Tm*) [76]. Thermal stability curves for BSA-complexes and BSA alone were plotted from 15 to 95 °C, as shown in Fig. 10. The melting temperature (*Tm*) of BSA was estimated in 72.1 °C and in the presence of complexes **1**–**4**, temperature varied from 67.2 to 75.4 °C, which indicates no significant increase in BSA stability. The addition of complexes **1**–**4** did not increase the melting temperature (*Tm*) of BSA. In sum, the CD spectra and thermal stability results indicate that there is no interaction between BSA and complexes **1**–**4**.

4. Summary and conclusions

In line with virtually all type A complexes with pyridine or small-substituents pyridine derivatives [10], **1**, **3** and **4** show no cytotoxicity, while **2** (in DMSO) shows some activity, attributable most likely to just the **meapy**. Our DNA interaction tests provide evidence for interaction with DNA and lack of protein interactions with BSA. Of the possible modes of interaction (Fig. 5), only non-covalent interactions need be considered for the measured interaction strengths. Intercalation can be ruled out definitively by EtBr fluorescence and the DNA solution viscosity measurements. Since these small molecules are not optimal for groove binding (which depends on strong dispersive interactions) the most likely interaction is electrostatic binding between the partly hydrolyzed mono-cationic forms of complexes **1**–**4**. Whereas it had been hoped

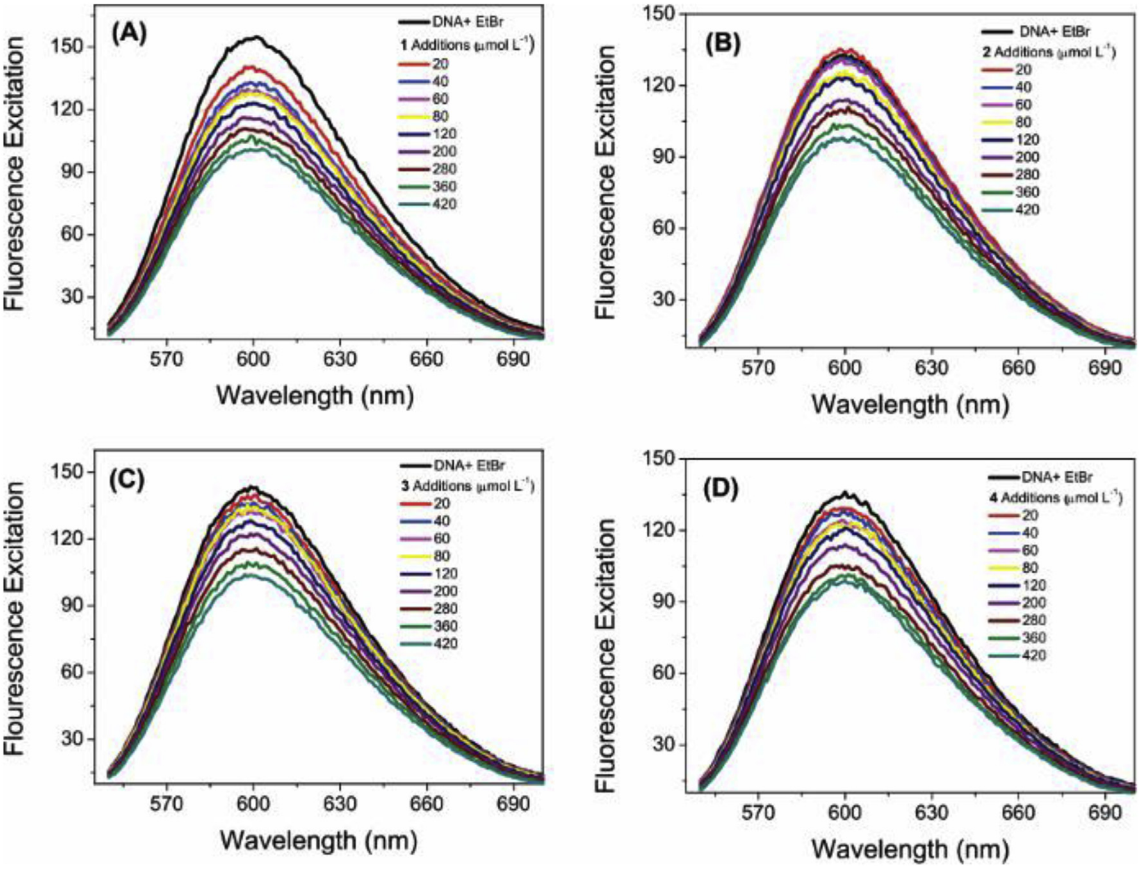

Fig. 8. Emission spectra of the EtBr/CT-DNA system, with successive additions of the complexes: (A) complex **1**; (B) complex **2**; (C) complex **3** and (D) complex **4**. Confirmed dilution effect after successive additions to PBS buffer.

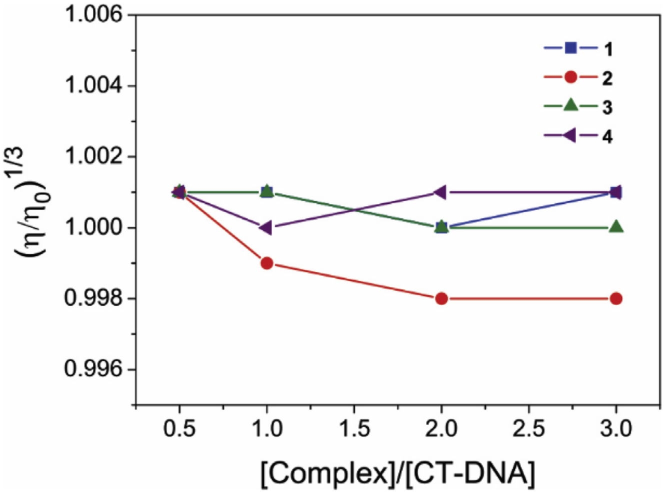

Fig. 9. Viscosity graph plotting the increase of the concentration of the complexes *vs.* the relative viscosity of the CT-DNA (20 μmol L^{-1}) at 25 °C.

that the benzyl group in **3** would be optimal for intercalation with DNA, apparently all these complexes pre-associate with the DNA backbone but do not proceed to intercalative or covalent linkage. Since our measurements show relatively slow rates of hydrolysis, the low activity of **1**–**4** may be due to lower than expected concentrations of active species in the conducted assays.

Table 4

Cytotoxicity results for 1–4 on HeLa, HEp-2, B16F10 and Vero cell lines, after 24 h incubation performed in DMSO solution or in aqueous buffer.

Complex	IC$_{50}$ (μmol L^{-1})			
	HeLa	HEp-2	B16F10	Vero
1 – DMSO [a]	>500	>500	>500	>500
2 – DMSO [a]	346 ± 3	>500	–	–
3 – DMSO [a]	>500	–	–	–
4 – DMSO [a]	>500	–	–	–
1 [b]	–	>630	–	–
2 [b]	–	>600	>600	–
3 [b]	–	>600	–	–
4 [b]	–	>650	–	–

[a] From DMSO stock solution; displacement of L by DMSO-S is assumed.

[b] Test performed using an aqueous buffer stock solution.

This study also provides valuable evidence for the high redox-stability of type-A [(η^6-*p*-cymene)RuCl$_2$L] complexes and provides the first detailed computational investigation of the electronic structures of this class of complex. These provide insights into the unusual voltammetry of oxidation and the assignment of electronic absorption spectra, results which we hope will be generally useful for the further development of organometallic ruthenium-based cytotoxic agents. Finally, our work confirms the unsuitability of the standard MMT protocol for cytotoxicity testing using DMSO to prepare stock solutions for κ^1-pyridyl type A complexes.

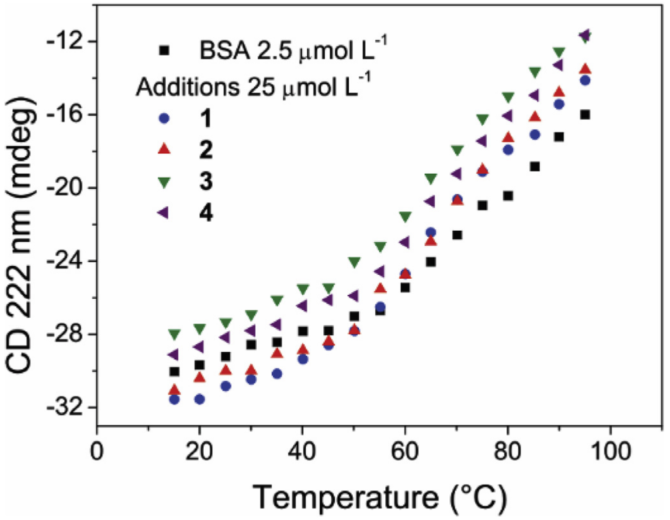

Fig. 10. CD spectra monitoring thermal denaturation of BSA in PBS buffer (pH 7.6) in the presence and absence of the $[(\eta^6\text{-}p\text{-cymene})RuCl_2(L)]$ series. Temperature range (15–90 °C).

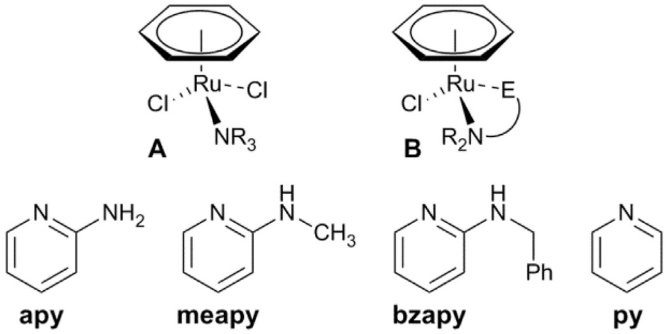

Chart 1. Structure types and ligands of importance to this work.

Acknowledgments

The authors thank the Brazilian agencies (CNPq PVE 401271/2014-5 and CAPES) for generous financial support through grants and scholarships. We acknowledge the Laboratory of Spectroscopy and Calorimetry at Brazilian Biosciences National Laboratory (LNBio), CNPEM, Campinas, Brazil for their support with the use of the spectropolarimeter and Prof. Christiane Philippini F. Borges from UEPG for providing access to the Fluorescence Spectrophotometer. We thank the University of Lethbridge for purchasing the SuperNova X-ray diffractometer and the anonymous referees for directing us to the literature regarding unsuitability of DMSO in the MMT protocols.

Appendix A. Supplementary data

Supplementary data to this article can be found online at https://doi.org/10.1016/j.jorganchem.2018.11.036.

References

[1] L. Zeng, P. Gupta, Y. Chen, E. Wang, L. Ji, H.Z.S. Chen, Chem. Soc. Rev. 46 (2017) 5771–5804.

[2] U. Ndagi, N. Mhlongo, M.E. Soliman, Drug Des. Dev. Ther. 11 (2017) 599–616.

[3] B.S. Murray, M.V. Babak, C.G. Hartinger, P.J. Dyson, Coord. Chem. Rev. 306 (2016) 86–114.

[4] J.K. Liang, H.J. Zhong, G. Yang, K. Vellaisamy, D.L. Ma, C.H. Leung, J. Inorg. Biochem. 177 (2017) 276–286.

[5] P. Zhang, P.J. Sadler, J. Organomet. Chem. 839 (2017) 5–14.

[6] C.S. Allardyce, P.J. Dyson, Dalton Trans. 45 (2016) 3201–3209.

[7] E. Alessio, Eur. J. Inorg. Chem. (2017) 1549–1560.

[8] P. Jia, R. Ouyang, P. Cao, X. Tong, X. Zhou, T. Lei, S. Zhou, J. Coord. Chem. 70 (2017) 2175–2201.

[9] B. Therrien, Coord. Chem. Rev. 253 (2009) 493–519.

[10] We Have Identified about 20 Complexes in This Category for Which Cytotoxicity Has Been Investigated by a SciFinder Search of the Chemical Abstracts Database. This information has been compiled in the Electronic Supporting Information (SI).

[11] R. Sàez, J. Lorenzo, M.J. Prieto, M. Font-Bardia, T. Calvet, N. Omeñaca, V. Moreno, J. Inorg. Biochem. 136 (2014) 1–12.

[12] J. Grau, V. Noe, C. Ciudad, M.J. Prieto, M. Font-Bardia, T. Calvet, V. Moreno, J. Inorg. Biochem. 109 (2012) 72–81.

[13] M.V. Babak, D. Plazuk, S.M. Meier, H.J. Arabshahi, J. Reynisson, B. Rychlik, A. Blauz, K. Szulc, M. Hanif, S. Strobl, A. Roller, B.K. Keppler, C.G. Hartinger, Chem. Eur J. 21 (2015) 5110–5117.

[14] K.S.A.M. Shweshein, F. Andric, A. Radoicic, M. Zlatar, M. Gruden-Pavlovic, Z. Tesic, D. Milojkovic-Opsenica, Sci. World J. 2014 (2014) 1–10.

[15] N. Gligorijević, S. Aranđelović, L. Filipović, K. Jakovljević, R. Janković, S. Grgurić-Šipka, Ž.L. Tešić, J. Inorg. Biochem. 108 (2012) 53–61.

[16] S. Grgurić-Šipka, I. Ivanović, G. Rakić, N. Todorović, N. Gligorijević, S. Radulović, Ž.L. Tešić, Eur. J. Med. Chem. 45 (2010) 1051–1058.

[17] K.G. Liu, X.Q. Cai, X.C. Li, D.A. Qin, M.L. Hu, Inorganica Chim. Acta. 388 (2012) 78–83.

[18] M. Patra, T. Joshi, V. Pierroz, K. Ingram, M. Kaiser, S. Ferrari, G. Gasser, Chem. Eur J. 19 (2013) 14768–14772.

[19] I. Ivanović, S. Grgurić-Šipka, N. Gligorijević, S. Radulović, A. Roller, Ž.L. Tešić, B.K. Keppler, J. Serb. Chem. Soc. 76 (2011) 53–61.

[20] T. D. Aicher, S. A. Boyd, M. J. Chicarelli, K. R. Condroski, R.J. Hinklin, A. Singh, US Pat. 20090156603 2007.

[21] G.R. Lawton, H.R. Ranaivo, L.K. Chico, H. Ji, F. Xue, P. Martásek, L.J. Roman, D.M. Watterson, R.B. Silverman, Bioorg. Med. Chem. 17 (2009) 2371–2380.

[22] High Cytotoxic Activity of Complex **4** towards HCT-116 Reported in Ref [13] has recently been contradicted by ref [25].

[23] C.A. Vock, C. Scolaro, A.D. Phillips, R. Scopelliti, G. Sava, P.J. Dyson, J. Med. Chem. 49 (2006) 5552–5561.

[24] J. Zhao, K.E. Prosser, S.W. Chang, S.P. Zakharia, C.J. Walsby, Dalton Trans. 45 (2016) 18079–18083.

[25] J. Zhao, D. Zhang, W. Hua, W. Li, G. Xu, S. Gou, Organometallics 37 (2018) 441–447.

[26] F. Schmitt, P. Govindaswamy, O. Zava, G. Süss-Fink, L. Juillerat-Jeanneret, B. Therrien, J. Biol. Inorg. Chem. 14 (2009) 101–109.

[27] S. Richter, S. Singh, D. Draca, A. Kate, A. Kumbhar, A.S. Kumbhar, Hey-Hawkins, Dalton Trans. 45 (2016) 13114–13125.

[28] P. Chuklin, V. Chalermpanaphan, T. Nhukeaw, S. Saithong, K. Chainok, S. Phongpaichit, N. Leesakul, J. Organomet. Chem. 846 (2017) 242–250.

[29] A. Inagaki, D.G. Musaev, T. Toshifumi, H. Suzuki, K. Morokuma, P.J. Rensburg, W. Steynberg, Organometallics 22 (2003) 1718–1727.

[30] W. Janse van Rensburg, P.J. Steynberg, W.H. Meyer, M.M. Kirk, G.S. Forman, J. Am. Chem. Soc. 126 (2004) 14332–14333.

[31] D. Benitez, W.A. Goddard, J. Am. Chem. Soc. 127 (2005) 12218–12219.

[32] C. Kreitner, E. Erdmann, W.W. Seidel, K. Heinze, Inorg. Chem. 54 (2015) 11088–11104.

[33] D. Das, A. Dutta, P. Mondal, Comput. Theor. Chem. 1072 (2015) 28–36.

[34] M.A. Bennett, T.W. Matheson, J. Organomet. Chem. 175 (1979) 87–93.

[35] B.S. Jensen, J.S. Rodger, D.M. Spicer, J. Organomet. Chem. 556 (1998) 151–158.

[36] D.D. Perrin, W.L.F. Armarego, Pergamon Press, New York (1988).

[37] W.J. Geary, Coord. Chem. Rev. 7 (1971) 81–122.

[38] M.J. Frisch, G.W. Trucks, H.B. Schlegel, G.E. Scuseria, M.A. Robb, J.R. Cheeseman, G. Scalmani, V. Barone, G.A. Petersson, H. Nakatsuji, X. Li, M. Caricato, A. Marenich, J. Bloino, B.G. Janesko, R. Gomperts, B. Mennucci, H.P. Hratchian, J.V. Ortiz, A.F. Izmaylov, J.L. Sonnenberg, D. Williams-Young, F. Ding, F. Lipparini, F. Egidi, J. Goings, B. Peng, A. Petrone, T. Henderson, D. Ranasinghe, V.G. Zakrzewski, J. Gao, N. Rega, G. Zheng, W. Liang, M. Hada, M. Ehara, K. Toyota, R. Fukuda, J. Hasegawa, M. Ishida, T. Nakajima, Y. Honda, O. Kitao, H. Nakai, T. Vreven, K. Throssell, J.A. Montgomery, Jr, J.E. Peralta, F. Ogliaro, M. Bearpark, J.J. Heyd, E. Brothers, K.N. Kudin, V.N. Staroverov, T. Keith, R. Kobayashi, J. Normand, K. Raghavachari, A. Rendell, J.C. Burant, S.S. Iyengar, J. Tomasi, M. Cossi, J.M. Millam, M. Klene, C. Adamo, R. Cammi, J.W. Ochterski, R.L. Martin, K. Morokuma, O. Farkas, J.B. Foresman, D.J. Fox, Gaussian, Inc., Wallingford CT, (2016).

[39] M. Sekiya, T. Noro, T. Koga, T. Shimazaki, Theor. Chem. Acc. 131 (2012) 1247.

[40] R. Aronson, M.R.J. Elsegood, J.W. Steed, D.A. Tocher, Polyhedron 10 (1991) 1727–1732.

[41] M.A. Bennett, A.K. Smith, Dalton Trans. 2 (1974) 233–241.

[42] A. Rodriguez-Barzano, J.D.A. Fonseca, A. John Blacker, P.C. McGowan, Eur. J. Inorg. Chem. 11 (2014) 1974–1983.

[43] M.E. Reichmann, S.A. Rice, C.A. Thomas, P.A. Doty, J. Am. Chem. Soc. 76 (1954) 3047–3053.

[44] N. Mudasir, H. Yoshioka, H. Inoue, J. Inorg. Biochem. 77 (1999) 239–247.

[45] J.L. García-Giménez, G. Alzuet, M. Gonzáles-Alvarez, M. Liu-Gonzáles,

A. Castiñeiras, J. Borrás, J. Inorg. Biochem. 103 (2009) 243–255.
[46] F. Denizot, R. Lang, J. Immunol. Methods 89 (1986) 271–277.
[47] F.H. Allen, Acta Crystallogr. Sect. B Struct. Sci. 58 (2002) 380–388.
[48] F. White, P. Sadler, M. Melchart, CSD Private Communication, 2015.
[49] C.M. Standfest-Hauser, K. Mereiter, R. Schmid, K. Kirchner, Dalton Trans. 11 (2003) 2329–2334.
[50] X.W. Yan, Y.R. Xie, Z.M. Jin, M.L. Hu, L.P. Zhou, Appl. Organomet. Chem. 32 (2018) 3923.
[51] K. Nakamoto, M. Margoshes, R.E. Rundle, J. Am. Chem. Soc. 77 (1955) 6480–6486.
[52] Thus, unlike many arene-Ru complexes investigated for cytotoxicity, 2-aminopyridine complexes do not have the high-lying filled and low-lying empty ligand π-orbitals found e.g. in bipyridyl-type complexes. It is therefore not possible to interpret electronic spectra or voltammetry experiments analogously to those systems that have 'redox-non-innocent' ligands. However, as noted in the section on voltammetry, this situation appears to change in oxidized states.
[53] P. Hosseinzadeh, Y. Lu, Biochim. Biophys. Acta Bioenerg. 1857 (2016) 557–581.
[54] While there is no direct expectation from the electronic structure calculations that the arene ligand should be displaced, an oft-quoted rationalization for irreversible oxidation processes, the bond strength to the *p*-cymene group may be weakened in such 17*e* complexes as evidenced by longer Ru–cymene-ring-centroid distances (see Figure S10 in the SI.).
[55] R.S. Nicholson, Anal. Chem. 38 (1966) 1406, 1406.
[56] B. Dražić, S. Grgurić-Šipka, I. Ivanović, Ž.L. Tešić, G. Popović, J. Iran. Chem. Soc. 9 (2012) 7–12.
[57] G. Gasser, N. Metzler-Nolte, Curr. Opin. Chem. Biol. 16 (2012) 84–91.
[58] A.F. Peacock, P.J. Sadler, Chem. Asian J. 3 (2008) 1890–1899.
[59] A.M. Pyle, J.P. Rehmann, R. Meshoyrer, C.V. Kumar, N.J. Turro, J. K Barton, J. Am. Chem. Soc. 111 (1989) 3051–3058.
[60] E.C. Long, J.K. Barton, Acc. Chem. Res. 23 (1990) 271–273.
[61] R.N. Irobalieva, J.M. Fogg, D.J. Catanese, T. Sutthi Butpong, M. Chen, A.K. Barker, S.J. Ludke, S.A. Harris, M.F. Schmid, W. Chiu, L. Zechi Edrich, Nat. Commun. 6 (2015) 8440.
[62] G. Pratviel, J. Bernadou, B. Meunier, Adv. Inorg. Chem. 45 (1998) 251–312.
[63] R. Amutha, V. Subramanian, B.U. Nair, Chem. Phys. Lett. 344 (2001) 40–48.
[64] T. Afrati, A.A. Pantazaki, C. Dendrinou-Samara, C. Raptopoulou, A. Terzis, D.P. Kessissoglou, Dalton Trans. 39 (2010) 765–775.
[65] Y.M. Chang, C.K.M. Chen, M.H. Hou, Int. J. Mol. Sci. 13 (2012) 3394–3413.
[66] N. Shahabadi, S. Kashanian, M. Khosravi, M. Mahdavi, Trans. Met. Chem. 35 (2010) 699–705.
[67] G. R. Bishop, J. B. Chaires, John Wiley & Sons Inc., New York, (2002).
[68] A. Rodger, B. Nordén, Oxford University Press, 1 (1997).
[69] L.W. Yielding, D.E. Graves, B.R. Brown, K.L. Yielding, Biochem. Biophys. Res. Commun. 30 (1979) 424–432.
[70] S. Moon, M. Hanif, M. Kubanik, H. Holtkamp, T. Söhnel, S.M. Jamieson, C.G. Hartinger, ChemPlusChem 80 (2015) 231–236.
[71] Q.A. Paula, A.A. Batista, E.E. Castellano, J. Ellena, J. Inorg. Biochem. 90 (2002) 144–148.
[72] J.A. Davies, Adv. Inorg. Chem. 24 (1981) 115–187.
[73] R.E. Morris, E.R. Aird, P. del Socorro Murdoch, H. Chen, J. Cummings, N.D. Hughes, S. Parsons, A. Parkin, G. Boyd, J.I. Duncan, P.J. Sadler, J. Med. Chem. 44 (2001) 3616–3621.
[74] R.E. Aird, J. Cummings, A.A. Ritchie, M. Muir, R.E. Morris, H. Chen, D.I. Jodrell, Br. J. Cancer. 86 (2012) 1652.
[75] Patra et al. Have Reported that DMSO Will Displace Monodentate Pyridine Ligands in Type-A Complexes and since DMSO Was Employed as the Transfer Vector for the Metal Complexes to the Biological Media in All These Tests, the Possibility Exists that it Is the Aminopyridines that Are the Active Agents – see reference [18].
[76] N.J. Greenfield, Nat. Protoc. 1 (2006) 2876.